scientific reports

Check for updates

OPEN

Paramagnetic defects and luminescence in praseodymium-activated alkaline earth pyrophosphates

Andris Antuzevics[1]✉, Didzis Salnajs[1], Guna Doke[1,2], Guna Krieke[1,2], Inga Pudza[1], Aleksandr Kalinko[1], Alexei Kuzmin[1], Nadiia Rebrova[3], Przemysław J. Dereń[3], Sapargali Pazylbek[2] & Aleksej Zarkov[2]

Establishing defect-property systematics in complex materials remains an elusive challenge, requiring complementary spectroscopic techniques and correlated investigations across chemically related host lattices. This study presents a systematic overview of defect-mediated charge trapping and recombination luminescence in Pr^{3+}-activated alkaline earth pyrophosphates ($X_2P_2O_7$; X = Ca, Sr, Ba). Phase composition and dopant incorporation are analysed using powder X-ray diffraction (XRD), X-ray absorption (XANES), and photoluminescence spectroscopy techniques. All $X_2P_2O_7:Pr^{3+}$ materials exhibit optical transitions in both the ultraviolet (UV) and visible (VIS) spectral regions, while $Sr_2P_2O_7$ and $Ba_2P_2O_7$ additionally show blue-to-UV-C upconversion potential. Charge trapping can be initiated by either X-ray or UV-C excitation, filling trapping states over a broad range of activation energies, with differences between the hosts reflected in the relative populations of shallow and deep traps. In $Sr_2P_2O_7:Pr^{3+}$, 444 nm excitation can additionally populate charge traps and generate UV–VIS persistent luminescence via an excited-state absorption (ESA) mechanism. Electron paramagnetic resonance (EPR) measurements reveal multiple phosphorus-related radicals, which, based on multifrequency spectra simulations, are assigned to PO_4^{2-}-type and PO_3^{2-}-type centres. The annealing kinetics of these radicals span over a 25–300 °C range and are partially correlated with maxima observed in TSL glow curves. These results establish a link between phosphorus-centred defects and recombination luminescence, providing a framework for defect-engineered phosphate materials.

Keywords Electron spin resonance (ESR), Afterglow, Long-lasting luminescence, Thermoluminescence, Radiation-induced radicals

Phosphate-based materials constitute an important class of functional ceramics due to their high physicochemical and thermal stability, relatively simple synthesis techniques, tuneable optical properties, and ability to accommodate a wide range of intrinsic and extrinsic defects. Central to the design of luminescent materials is the interplay between dopant electronic states and charge carrier trapping sites, which together control energy storage and delayed or stimulated emission characteristics. Recent advances in rare-earth-activated phosphate materials have shown the role of these defect-mediated processes in various luminescence mechanisms[1–7]. For example, Zhao et al. reported tuning of Eu^{2+} persistent luminescence emission characteristics through compositional modifications of $Ca_{10}M(PO_4)_7$ (M = Li, Na, K)[2]. In Gd^{3+}-doped $Sr_3(PO_4)_2$ and $LiCaPO_4$, X-ray-generated electron–hole pairs fill both shallow and deep traps, where de-trapping of the former results in exceptionally long UV-B persistent luminescence, whereas the accumulation of stable traps gives rise to sample colouration[3,4]. Pr^{3+}-doped phosphates have been reported to simultaneously offer multiple luminescence pathways extending from UV-C up to red spectral regions[5–7]. Notably, X-ray excitation of $Sr_3(PO_4)_2:Pr^{3+}$ provides multicolour persistent luminescence and optically stimulated luminescence (OSL) under 980 nm excitation[5]. In $LuPO_4:Pr^{3+}$, solar-blind OSL can be triggered by ambient light, which enables "glow-in-the-daylight" applications[6]. A unique combination of blue-light-driven UV-C up-conversion with X-ray-excited persistent luminescence within

[1]Institute of Solid State Physics, University of Latvia, Kengaraga 8, Riga 1063, Latvia. [2]Institute of Chemistry, Vilnius University, Naugarduko 24, 03225 Vilnius, Lithuania. [3]Institute of Low Temperature and Structure Research, Polish Academy of Sciences, 50-422 Wrocław, Poland. ✉email: andris.antuzevics@cfi.lu.lv

a single host lattice has been achieved in eulytite-type phosphates, highlighting their potential use in next-generation anticounterfeiting and information encryption technologies[7].

Within the broader class of phosphate materials, pyrophosphates represent a versatile platform for luminescence engineering[8–17]. Structurally, the pyrophosphate group $[P_2O_7]^{4-}$ consists of two corner-sharing $[PO_4]^{3-}$ tetrahedra linked via a bridging oxygen, providing a chemically flexible framework capable of accommodating defects and facilitating charge compensation. These compounds can be crystallised into several stable polymorphic modifications with distinct local environments for pyrophosphate groups and multiple available cation sites[13–15]. TSL and magnetic resonance studies of $Ca_2P_2O_7$ and $Sr_2P_2O_7$ show potential for radiation dosimetry due to the dose-dependent filling of charge traps[10–13]. Recently, Pr^{3+}-doped pyrophosphates have received considerable interest due to deep UV-C emission associated with the $[Xe]4f^15d^1 \rightarrow [Xe]4f^2$ transitions and excellent trap storage properties[12,15–17]. X-ray charging of $Ca_2P_2O_7$:Pr^{3+} produces persistent luminescence, which can be stimulated both thermally and optically by 980 nm radiation[16], whereas $Sr_2P_2O_7$:Pr^{3+} additionally exhibits mechanoluminescent behaviour[12]. A broader overview of luminescence and defect properties in Pr^{3+}-doped pyrophosphate materials would thus be timely.

Despite considerable progress in characterising luminescence processes and charge trap activation energies in phosphate-based materials, identification of the trapping centres remains challenging. The associated electron traps are frequently discussed in terms of oxygen-vacancy-related defects[2,5,6,9]; however, the whole picture likely involves charge localisation across phosphorus oxyanions $[P_xO_y]^{z-}$ rather than isolated point defects. This complexity is further exacerbated by the inherent limitations of conventional optical techniques, which provide limited insight into the electronic structure of the underlying defects. In this context, electron paramagnetic resonance (EPR) spectroscopy offers a powerful and complementary approach, enabling direct detection and identification of paramagnetic centres through their characteristic g-tensors and hyperfine interactions[18]. When correlated with luminescence techniques, EPR data can help establish relationships between identified defect centres and recombination processes.

This study systematically investigates photoluminescence, up-conversion luminescence, thermally stimulated luminescence (TSL), and persistent luminescence in Pr^{3+}-activated alkaline earth pyrophosphates ($X_2P_2O_7$:Pr^{3+}; X = Ca, Sr, Ba). Radiation-induced charge trapping is analysed using simulations of multifrequency EPR spectra and correlated with recombination luminescence processes. $Sr_2P_2O_7$:Pr^{3+} is established as a prospective material for UV–VIS persistent luminescence and optically stimulated luminescence (OSL) applications.

Materials and methods

Material synthesis

Three series of $X_2P_2O_7$:Pr^{3+} (XPP; X = Ca, Sr, Ba) powders with Pr content of 0.0, 0.2, 0.5, 1.0, 1.5, 2.0, and 3.0 mol% were synthesised by the solid-state reaction method. The doping level is indicated with respect to an appropriate alkaline earth metal ion. Calcium nitrate tetrahydrate ($Ca(NO_3)_2{\cdot}4H_2O$, Carl Roth, > 99%), strontium nitrate ($Sr(NO_3)_2$, Thermo Scientific, ≥ 99%), and barium nitrate ($Ba(NO_3)_2$, Thermo Scientific, 99%) were used for the synthesis of $Ca_2P_2O_7$, $Sr_2P_2O_7$, and $Ba_2P_2O_7$, respectively. Diammonium hydrogen phosphate ($(NH_4)_2HPO_4$, Carl Roth, > 98%) and praseodymium(III) nitrate pentahydrate ($Pr(NO_3)_3{\cdot}5H_2O$, Thermo Scientific, 99.9%) were used as P and Pr sources. For the synthesis, stoichiometric amounts of appropriate metal nitrates and $(NH_4)_2HPO_4$ were mixed in an agate mortar. The obtained mixture was transferred to a porcelain crucible and heated in a muffle furnace at 500 °C for 5 h in air. The obtained intermediate product was ground in a mortar and annealed at 1100 °C for 5 h in air. After annealing, the furnace was allowed to cool down naturally. The $Ca_2P_2O_7$, $Sr_2P_2O_7$, and $Ba_2P_2O_7$ samples are hereafter abbreviated as CPP, SPP, and BPP, respectively.

Characterisation

The phase composition of the powder samples was determined using a Rigaku MiniFlex II X-ray diffractometer equipped with a Ni-filtered Cu Kα radiation source working in Bragg–Brentano (θ/2θ) geometry.

The Pr L_3-edge X-ray absorption spectra of $X_2P_2O_7$:0.5% Pr^{3+} (X = Ca, Sr, Ba) were collected at room temperature at the DESY PETRA III P64 undulator beamline[19]. The storage ring operated at 6 GeV and 120 mA in multi-bunch mode. The incident photon energy was selected using a liquid-nitrogen-cooled Si(111) double-crystal monochromator, with higher harmonics suppressed by silicon mirrors. The incident X-ray intensity was monitored by a nitrogen-filled ionization chamber, and the fluorescence from the sample was detected using a passivated implanted planar silicon (PIPS) detector placed at 90° from the incident beam direction. Samples were measured as pressed pellets prepared with cellulose. The Pr L_3-edge X-ray absorption near-edge structures (XANES) were extracted using the XAESA software[20].

Photoluminescence emission spectra were acquired using an Edinburgh Instruments FLS1000 photoluminescence spectrometer equipped with a 450W Xe arc lamp for excitation and a photomultiplier tube R928P for signal acquisition. For measurement, the polycrystalline powders were pressed into stainless steel sample holders. Low-temperature site-selective spectrometry measurements were performed using the Advanced Research Systems DE202 N cold finger-type He cryostat. The samples were excited using a wavelength-tuneable pulsed solid-state laser Ekspla NT342/3UV. The emission signal was detected by an Andor iStar DH734-18F-A3 CCD camera coupled to an Andor SR-303i-B spectrometer.

The upconversion properties were measured using a McPherson spectrometer (Model 218) equipped with a photomultiplier tube insensitive to visible light (Hamamatsu R7154P). A diode laser with a wavelength of 444 nm and pulse duration of 6 ns (5W, Changchun new industries optoelectronics tech co. ltd) was used to obtain the upconversion emission spectra, while the decay curves of the upconversion emission were measured using the second harmonic of a Ti:sapphire laser pumped by the second harmonic of an Nd:YAG laser (LOTIS TII, Belarus).

X-ray excited luminescence (XRL) and TSL measurements were carried out using a Lexsyg research Fully Automated TL/OSL Reader from Freiberg Instruments GmbH. The irradiation was performed using an X-ray tube (40 kV, 0.5 mA, W-anode). Measurements were recorded either with a Hamamatsu R13456 PMT or an Andor Technology SR-303i-B spectrometer linked to a DV420A-BU2 CCD camera. During TSL measurements, the system was operated at a constant heating rate of 1 °C/s.

Persistent luminescence emission power density was measured using a PD300E-UV photodiode power sensor coupled to a Centauri console (Ophir Optronics Solutions), following a previously reported method[21]. Approximately 0.4 g of phosphor powder was pressed into a tablet with a diameter of 13 mm. The UV and visible emission regions were isolated using a 310 nm short-pass UV filter (Asahi Spectra) and a FEL0500 long-pass filter (Thorlabs), respectively. During all measurements, the distance from the sample to the detector was fixed at 30 mm.

EPR spectra were recorded with a Bruker ELEXSYS-II E500 spectrometer. Room-temperature (RT) measurements were performed at X-band (9.83 GHz) and Q-band (34.0 GHz). Low-temperature measurements (80 K) at X-band were carried out at 9.36 GHz using an Oxford Instruments liquid helium flow cryostat. A magnetic field modulation amplitude of 0.2 mT was applied in all experiments. Microwave power was optimised individually for each measurement series. Unless stated otherwise, radiation-induced radicals were generated by exposing the samples to X-rays (45 kV, 10 mA) for 10 min at room temperature; sample transfer to the EPR spectrometer was done in approximately 3 min. After irradiation, the samples were isochronally annealed in air using a custom-built furnace, with each annealing step maintained for 10 min. EPR spectra were simulated using the EasySpin software[22].

Results and discussion

Structural characterisation

Figure 1 shows representative powder X-ray diffraction (XRD) patterns for the investigated pyrophosphate materials. Good agreement with the reference data is observed, with no additional diffraction peaks detected for samples with Pr^{3+} concentration below 1.0%. The diffraction patterns were indexed, and phase composition was identified as tetragonal β-CPP, orthorhombic α-SPP and hexagonal σ-BPP, corresponding to ICDD PDF cards 04-009-8733, 04-013-9357, and 04-027-9304, respectively. For Pr^{3+} concentrations above 1 mol%, additional reflections appear in the diffraction patterns, which are consistent with the presence of minor $PrPO_4$ (01-083-0653) impurity phases in all hosts and $Sr_3(PO_4)_2$ (04-015-2023) in SPP, as determined from the Rietveld refinement. This behaviour suggests a limited solubility of rare-earth dopants in alkaline-earth pyrophosphate hosts.

The crystal structures of the identified phases differ significantly. Considering the large difference in ionic radii between Pr^{3+} (0.99 Å, CN = 6, to 1.18 Å, CN = 9) and P^{5+} (0.17 Å, CN = 4)[23], the incorporation of Pr^{3+} is expected to occur preferentially at the alkaline earth sites (Ca^{2+}, Sr^{2+}, or Ba^{2+}) rather than at the phosphorus sites. β-CPP crystallises in the tetragonal $P4_1$ (#76) space group and contains four crystallographically distinct Ca^{2+} sites with coordination numbers ranging from 7 to 9[24]. In contrast, α-SPP adopts an orthorhombic *Pnma* (#62) structure with two non-equivalent Sr^{2+} sites, both 9-coordinate[25], while σ-BPP crystallises in the hexagonal $P6_3m$ (#189) space group, where Ba^{2+} ions occupy two distinct sites with coordination numbers of 7 and 10[26]. The diversity of coordination environments and crystallographic sites provides a structural basis for the multiple local environments and defect configurations associated with Pr^{3+} incorporation.

The experimental Pr L_3-edge XANES spectra of XPP:0.5% Pr^{3+} (X = Ca, Sr, Ba) are shown in Fig. 2. They closely resemble the Pr L_3-edge XANES spectra of $Mg_3Lu_2Ge_3O_{12}$:1% Pr^{3+} and $Ca_2Al_2SiO_7$:3% Pr^{3+} reported in our previous studies[27,28]. The spectra are dominated by a strong maximum at about 5968 eV, the so-called "white line", attributed to the $2p_{3/2} \rightarrow 5d$ dipole-allowed transition, with the final excited state $4f^25d^1$ of Pr^{3+}. The shape and position of the white line indicate that praseodymium ions are predominantly present in the Pr^{3+} oxidation state. This conclusion is supported by comparison with Pr L_3-edge XANES spectra of praseodymium oxides PrO_2 (Pr^{4+})[29], Pr_2O_3 (Pr^{3+}), and Pr_6O_{11} (Pr^{4+})[30] as well as $PrVO_4$ (Pr^{3+})[31] and Pr^{3+}-doped borate glasses[30,31]. Note that the Ba L_1-edge XANES overlaps with the Pr L_3-edge in BPP:0.5% Pr^{3+}.

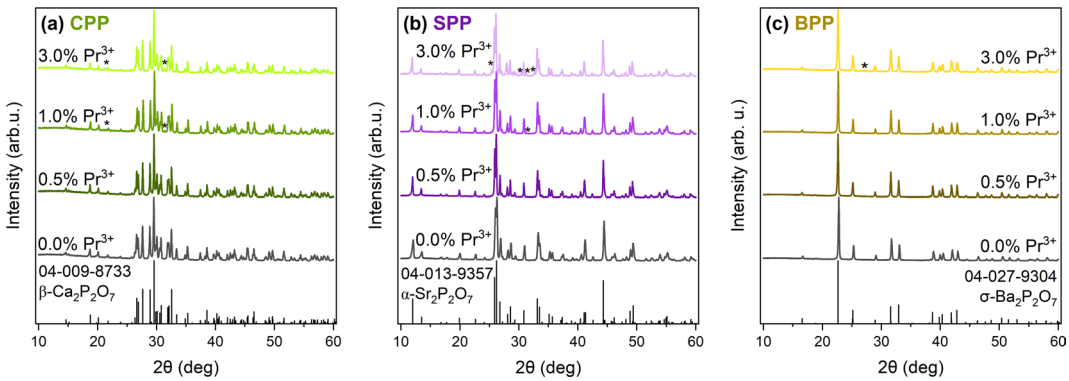

Fig. 1. XRD patterns of (**a**) CPP, (**b**) SPP, and (**c**) BPP; asterisks denote the impurity phases.

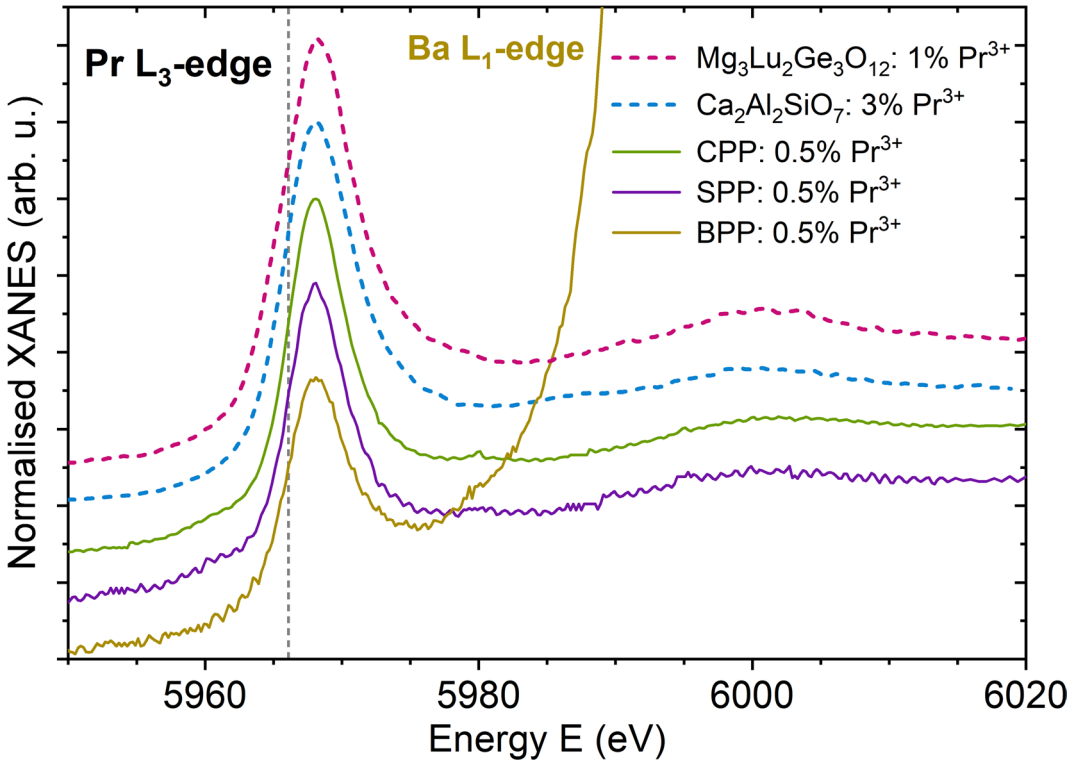

Fig. 2. The Pr L_3-edge XANES spectra of praseodymium in XPP:0.5% Pr^{3+} (X = Ca, Sr, Ba). The XANES spectra of $Mg_3Lu_2Ge_3O_{12}$:1% Pr^{3+}[27] and $Ca_2Al_2SiO_7$:3% Pr^{3+}[28] are shown for comparison. The beginning of the Ba L_1-edge at about 5958 eV is visible in XANES of $Ba_2P_2O_7$:0.5% Pr^{3+}. The position of the absorption edge is indicated by the dashed line.

Luminescence characterisation

Photoluminescence emission spectra of the investigated samples are shown in Fig. 3, with the UV emission region and visible emission regions presented separately and normalised for clarity. The UV emission was recorded under excitation at 224 nm, while the visible emission spectra were recorded using 442 nm excitation.

Under UV excitation, the CPP samples exhibit multiple emission bands centred at approximately 230 and 260 nm, corresponding to the allowed interconfigurational $4f^15d^1 \rightarrow 4f^2$ transitions of Pr^{3+}. These bands exhibit further splitting that is associated with transitions from the $4f^15d^1$ states to low-lying $4f^2$ multiplets, primarily $^3H_{4,5,6}$ and $^3F_2$[15,17,32].

In the visible region, the emission spectra are dominated by a series of emission lines centred at around 600 nm, arising primarily from the $^1D_2 \rightarrow {}^3H_4$ electronic transition. Additional emission bands observed at approximately 487, 644, 700, and 725 nm correspond to the Pr^{3+} $^3P_0 \rightarrow {}^3H_4$, $^3P_0 \rightarrow {}^3F_2$, $^1D_2 \rightarrow {}^3H_5$, and $^3P_0 \rightarrow {}^3F_4$ transitions, respectively[12,15,16]. The overall spectral profile varies noticeably between the different pyrophosphate hosts, reflecting differences in the local crystal field environment of Pr^{3+}.

Pyrophosphate samples were analysed using site-selective spectroscopy by measuring excitation and emission spectra at 10 K. At low temperatures, the narrowing of excitation and emission bands allows the selective excitation of emitting centres at specific lattice positions. The emission spectra of $^3P_0 \rightarrow {}^3H_4$ transitions excited by $^3H_4 \rightarrow {}^3P_1$, $^1I_6$, $^3P_2$ are shown in Fig. 4.

In all samples, variation of the excitation wavelength reveals multiple emission spectra, indicating the presence of Pr^{3+} ions in several local environments. In CPP, four well-resolved emission signals are observed, suggesting that Pr^{3+} is incorporated in at least four different positions (Fig. 4a). In SPP, spectra from at least two distinct Pr^{3+} positions are detected (Fig. 4b). The relatively narrow emission lines of CPP and SPP suggest that Pr^{3+} ions occupy well-defined and relatively ordered sites. In contrast, BPP exhibits broader emission bands that gradually shift with excitation wavelength (Fig. 4c), which is indicative of a distortion of local environments rather than the formation of discrete crystallographic sites. As discussed above, the relatively large Pr^{3+} ions are expected to substitute alkaline earth cation positions in the investigated pyrophosphates. The obtained results are consistent with Pr^{3+} replacing the available Ca^{2+} and Sr^{2+} positions in CPP and SPP, whereas the broad emission features observed in BPP suggest significant structural distortion. The coexistence of multiple Pr^{3+} positions in the XPP hosts indicates that the room temperature PL spectra shown in Figs. 3 and 5 likely consist of multiple overlapping emission signals.

Praseodymium is a unique activator that, when incorporated into wide-bandgap host matrices, can exhibit UV luminescence upon excitation with visible light[33]. This anti-Stokes process, involving the conversion of low-energy radiation to high-energy emission, is referred to as upconversion luminescence[34]. The wide bandgap of

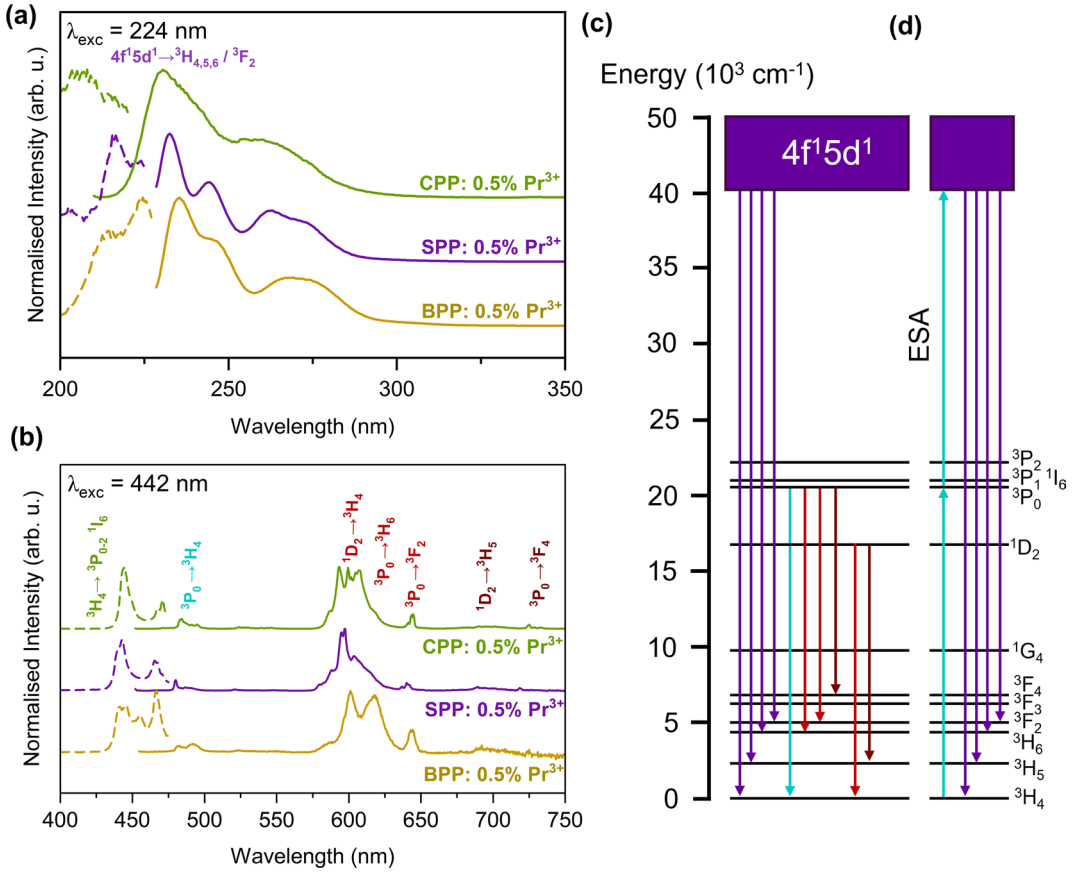

Fig. 3. Photoluminescence emission and excitation spectra using (**a**) $\lambda_{exc} = 224$ nm; $\lambda_{em} = 236$ nm and (**b**) $\lambda_{exc} = 442$ nm; λ_{em} for excitation spectra selected according to the $^1D_2 \rightarrow {}^3H_4$ transition of CPP, SPP, and BPP doped with 0.5% Pr^{3+}. Schematic energy level diagram of Pr^{3+} with potential (**c**) photoluminescence and (**d**) excited-state absorption upconversion luminescence mechanisms.

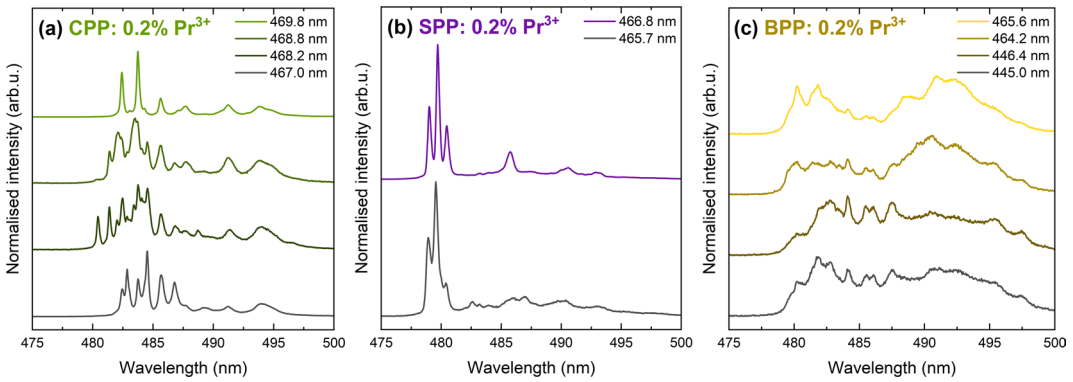

Fig. 4. Site-selective spectra of $^3P_0 \rightarrow {}^3H_4$ transitions in (**a**) CPP, (**b**) SPP, and (**c**) BPP doped with 0.2% Pr^{3+} detected at 10 K.

the investigated pyrophosphate hosts[15,35,36] enables efficient population of high-energy 5d states, resulting in ultraviolet emission under excitation at 444 nm (Fig. 5a). The observed broad emission band is attributed to interconfigurational $5d4f \rightarrow 4f^2$ (^3H_J, ^3F_J) transitions of Pr^{3+}[37]. The differences between the Stokes and anti-Stokes emission spectra (Figs. 3a and 5a) may arise from distinct excitation pathways. In the upconversion experiment, excitation at 444 nm populates the $^3P_2$ level of the Pr^{3+} ion, followed by rapid nonradiative relaxation to the $^3P_0$ state. Absorption of a second 444 nm photon then promotes the ion to the 4f5d configuration, corresponding to an effective excitation energy of approximately 42,930 cm^{-1} (≈ 232 nm). Consequently, Stokes excitation at

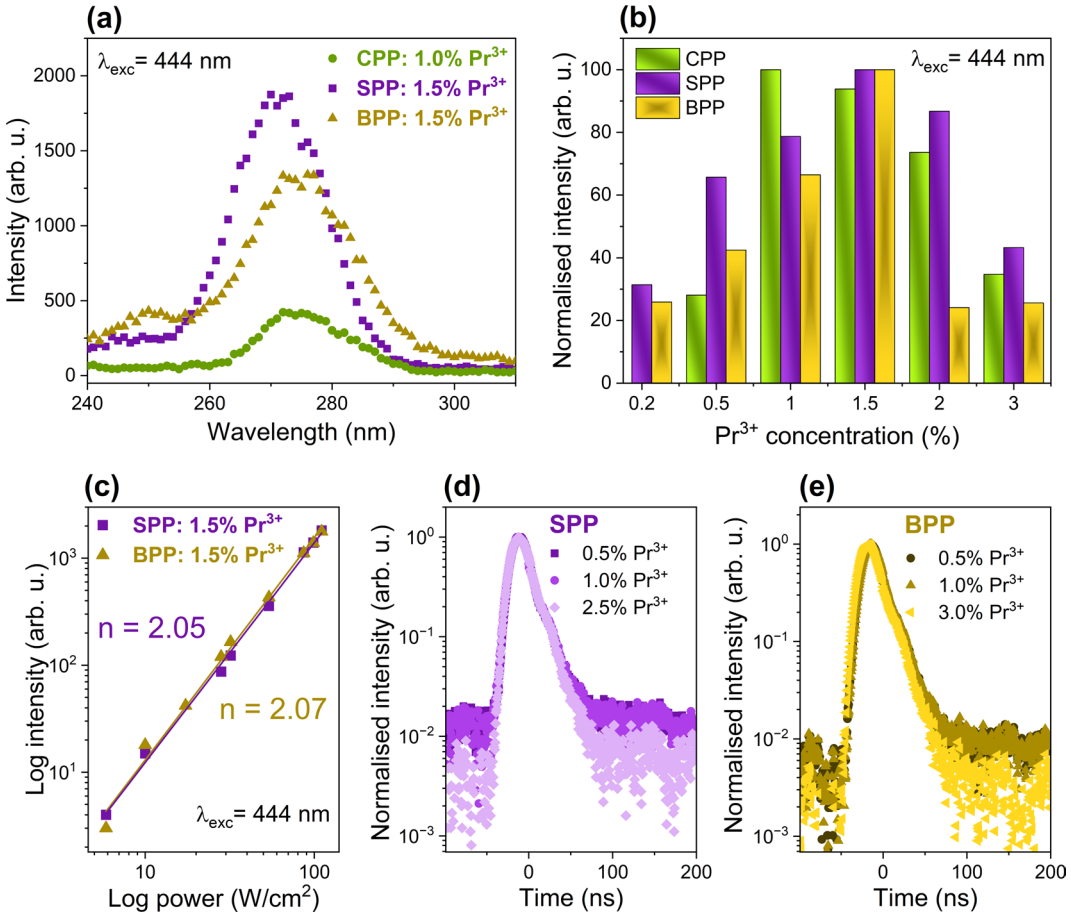

Fig. 5. Upconversion luminescence properties of XPP:Pr^{3+} (X = Ca, Sr, Ba): (**a**) emission spectra under 444 nm laser excitation; (**b**) dependence of the integral upconversion intensity (230–280 nm) on Pr^{3+} concentration; (**c**) upconversion intensity pump power dependence for SPP:1.5% Pr^{3+} and BPP:1.5% Pr^{3+}. Upconversion emission decay curves of (**d**) SPP:Pr^{3+} and (**e**) BPP:Pr^{3+} under pulsed excitation at 440 nm.

224 nm and anti-Stokes excitation at an effective wavelength of ≈ 232 nm populate different excited states, which may contribute to the observed spectral differences.

As shown in Fig. 3, the SPP and BPP emission spectra exhibit four well-resolved Pr^{3+} $4f5d$-$4f^2$ emission bands. The pronounced spectral resolution can be attributed to the low-symmetry crystal-field environment of the Pr^{3+} ions, which induces strong splitting of the 5d levels. Similar observations have been reported for YPO_4:Pr^{3+}, $LuPO_4$:Pr^{3+}, and $LiYF_4$:Pr^{3+}[37]. In contrast, the CPP host lattice provides a more symmetric local environment for Pr^{3+}, resulting in weaker crystal-field splitting and, consequently, less well-resolved emission features. The shape of the upconversion spectra further suggests that the observed emission may predominantly originate from Pr^{3+} centres occupying lattice sites with higher local symmetry. However, this interpretation remains tentative, as it cannot be directly verified from the Stokes-excited emission spectra alone.

The upconversion emission intensity depends strongly on the activator concentration (Fig. 5b). For SPP and BPP, the maximum intensity is observed at a Pr^{3+} concentration of 1.5%, whereas for CPP, the optimal concentration is 1.0%. This difference is likely related to the critical energy transfer distance between Pr^{3+} ions[38]. The number of photons involved in the upconversion mechanism n was determined by analysing the dependence of emission intensity I on the laser pump power P, following the relation $I \propto P^n$. The logarithmic plots of emission intensity versus pump power for BPP:1.5% Pr^{3+} and SPP:1.5% Pr^{3+} are shown in Fig. 5c. The slopes of these plots are approximately 2, indicating a two-photon upconversion mechanism.

For CPP:Pr^{3+}, the upconversion emission was too weak to reliably determine either the pump power dependence or the upconversion emission lifetimes. The decay curves for the upconversion emission of SPP and BPP are presented in Fig. 5d, e, and the corresponding lifetimes are summarised in Table 1. A slight decrease in lifetime with increasing activator concentration is observed, consistent with concentration quenching effects. The two most common upconversion luminescence mechanisms are excited-state absorption (ESA) and energy transfer upconversion (ETU). These mechanisms can be distinguished by luminescence kinetics. In the case of ESA, the lifetime of the upconversion luminescence corresponds directly to the lifetime of the emitting state, and the luminescence decays immediately after the excitation pulse. In contrast, the ETU mechanism exhibits more complex kinetics. Specifically, an initial rise in the luminescence intensity is observed, reflecting the population dynamics and lifetime of the intermediate energy level, followed by a generally longer decay

Pr^{3+} content	SPP τ_{uc}, ns	BPP τ_{uc}, ns
0.2%	–	18.7
0.5%	20.1	17.6
1.0%	19.4	17.9
1.5%	19.3	16.3
2.0%	18.6	15.8
3.0%	17.5	15.2

Table 1. Upconversion emission decay times of Pr^{3+} in SPP and BPP.

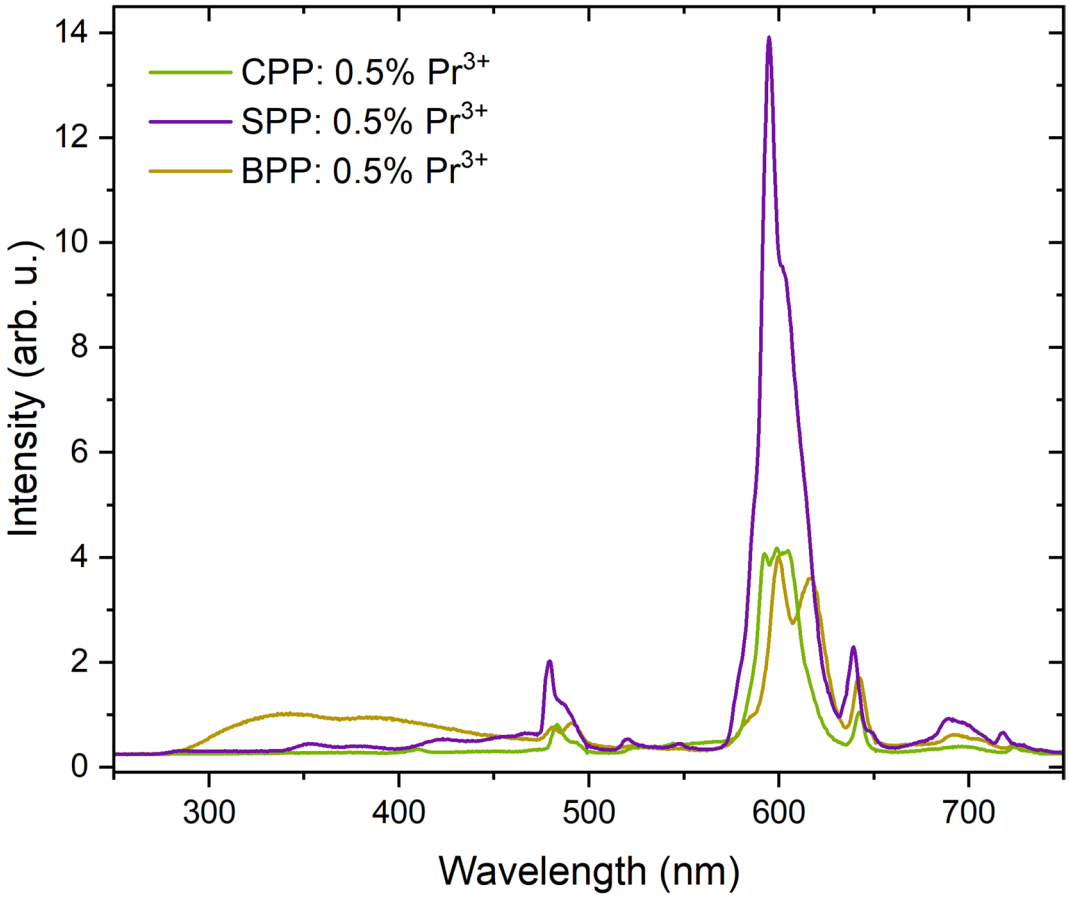

Fig. 6. XRL spectra of 0.5% Pr^{3+}-doped CPP, SPP, and BPP samples.

process than that observed for ESA[34]. The decay constant for ETU is related to approximately one-half of the lifetime of the intermediate state; in the investigated phosphors, the $^3P_0$ level acts as this intermediate state[39]. No measurable rise component was observed in the decay curves of SPP and BPP within the temporal resolution of the experiment. Moreover, since the measured upconversion luminescence lifetimes are extremely short—on the order of several tens of nanoseconds (Table 1)—and are comparable to the lifetime of the emitting excited state, the ESA mechanism is most likely responsible for the observed upconversion emission. A schematic illustration of this mechanism[39] is presented in Fig. 3d.

X-ray irradiation was carried out to generate electron–hole pairs in the XPP samples, enabling investigation of charge trapping and recombination processes via XRL and TSL techniques. During X-ray excitation, all doped samples exhibit emission spectra characteristic of Pr^{3+} ions (Fig. 6), consistent with the photoluminescence observations discussed above (Fig. 3), suggesting that Pr^{3+} ions act as the primary recombination centres under X-ray irradiation. Notably, no Pr^{3+}-related UV emission from the higher-lying 5d levels was observed. The absence of Pr^{3+} 4f5d–4f emission under X-ray excitation suggests that the X-ray-induced recombination process predominantly populates the lower-lying 4f excited states rather than the higher-energy 5d levels. Although radiation-induced colour centres could also contribute to suppression of the UV emission, such effects were not investigated in the present work. The only significant difference among samples is observed for BPP, where an

additional broad emission between 250 and 450 nm appears. This broadband feature is most likely associated with intrinsic host-related defects.

To characterise charge trapping processes, TSL analysis following X-ray irradiation was performed. The obtained TSL glow curves are depicted in Figs. 7 and S1. TSL glow curves of all samples reveal an intricate system of numerous semi-overlapping trapping states, with corresponding glow peaks appearing throughout the measured temperature range from room temperature to 350 °C. The approximate temperature maximum positions for the doped CPP samples are: 60, 110, 195, 240, 300 °C; for SPP: 65, 105, 150, 205, 285 °C; and for BPP: 55, 110, 185, 290 °C. The principal TSL glow peaks occur within comparable temperature ranges for all three hosts, suggesting that the corresponding trap activation energies are similar. The main difference between the sample groups is reflected in the relative intensities of the TSL glow peaks. In CPP, the TSL signal is dominated by high-temperature glow peaks, whereas in SPP the low-temperature glow peaks contribute more. These differences cannot be solely attributed to PL intensity dependence of Pr^{3+} (Fig. S2), but arise from variations in trap concentration, trap population after irradiation, and recombination efficiency. Generally, considering the overall TSL signal of the doped samples, the SPP samples exhibit the highest measured intensity, whereas the BPP samples show values approximately two orders of magnitude lower; therefore, trap generation/filling under X-rays is considerably higher for the SPP. When undoped samples are compared, it is evident that in all three cases, multiple charge traps are present across the measured temperature range; however, the SPP and BPP samples exhibit relatively weak TSL signal intensity, which increases significantly upon doping. By contrast, the undoped CPP sample has greater measured TSL intensity than the doped CPP samples, suggesting that doping redistributes trap populations and/or alters recombination pathways, leading to reduced radiative recombination from certain trapping states. As demonstrated in "$Sr_2P_2O_7$:0.5% Pr^{3+}" section, excitation of the Pr^{3+} electronic states can also populate trapping centres, indicating that the activator plays a more direct role in trapping processes than merely perturbing the host lattice indirectly.

For further insight into recombination processes, TSL spectra were recorded. Figure S3 depicts wavelength-resolved TSL contour plots of undoped CPP and 0.5% Pr^{3+}-doped XPP samples. All doped samples have characteristic Pr^{3+} luminescence bands; however, slight variations in the relative intensities of the emission bands are observed between samples, which can be attributed to differences in the host lattice affecting the crystal field around the Pr^{3+} ions. For SPP and BPP, only Pr^{3+} luminescence bands over the entire investigated temperature range are observed. In the case of SPP, not only is visible-range Pr^{3+} emission detected, but UV bands originating from 4f5d to 4f transitions are also observed. In contrast, the CPP samples exhibit an additional emission band at higher temperatures (~ 150 to 250 °C). This band exhibits a noticeable shift in its emission maximum position depending on Pr^{3+} doping. This emission is attributed to Mn^{2+} ions, whose luminescence is known to be highly sensitive to the local crystal field[40]. The presence of uncontrolled Mn^{2+} impurities in the CPP samples is likely introduced with the Ca precursors. This assignment is further supported by EPR measurements, which are discussed in the next section. The wavelength-resolved contour plots of undoped SPP and BPP samples (Fig. S4) exhibit weak, featureless luminescence likely originating from intrinsic defects and several trace impurities.

The 0.5% Pr^{3+}-doped CPP, SPP, and BPP samples were selected to determine the trap-depth values. The results are summarised in Figs. 8, S5, and Table 2. For analysis, two commonly used TSL methods were chosen: $T_{max}-T_{stop}$ and initial rise analysis (IRA)[41–43]. The $T_{max}-T_{stop}$ method was employed to probe the distribution of trapping states by progressively preheating the samples to increasing T_{stop} temperatures before to TSL measurement. This approach enables partial thermal cleaning of traps, allows evaluation of trap properties, and provides insight into the distribution and nature of trapping states. If T_{max} does not change with increased T_{stop}, the corresponding trapping state has a discrete activation energy (E_a) value, whereas if a quasi-continuous distribution of trapping states is present, T_{max} should increase proportionally with T_{stop}. The analysed samples do not fully fit either characteristic; however, T_{max} clearly divides into separate groups for each glow peak. The non-constant T_{max} for each glow peak is somewhat expected in the case of strong overlap of multiple glow peaks. Thus, it can be presumed that multiple discrete trapping states are present in each sample.

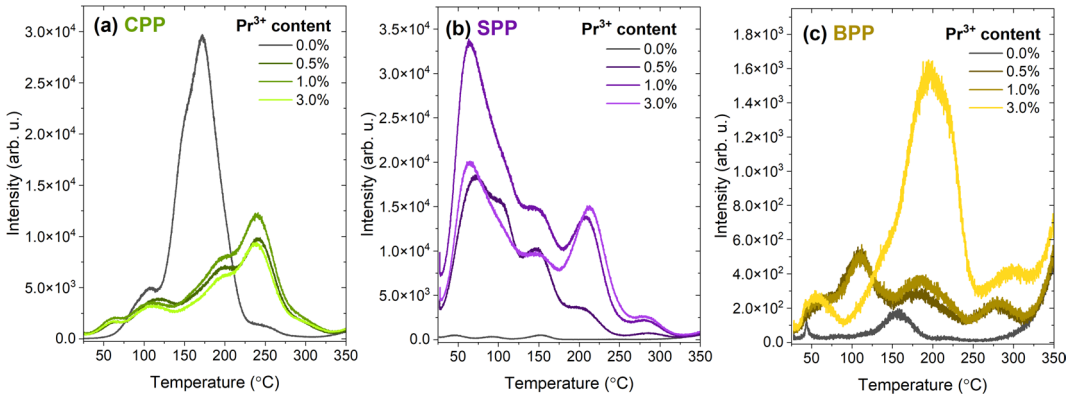

Fig. 7. TSL glow curves of the (**a**) CPP, (**b**) SPP, and (**c**) BPP samples after 15 s X-ray irradiation.

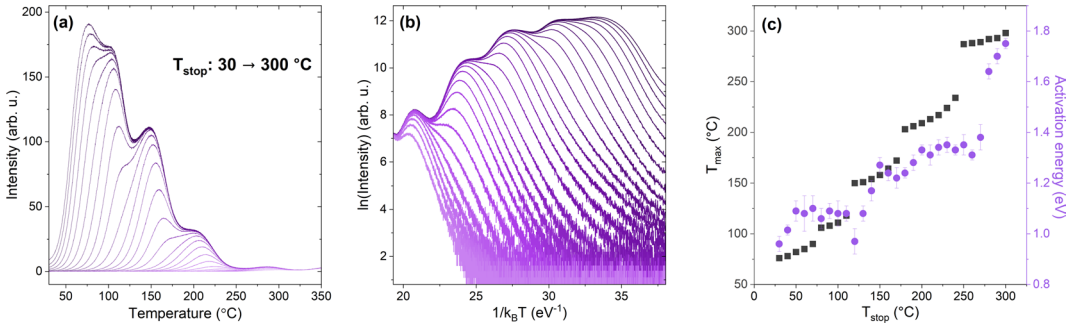

Fig. 8. (**a**) TSL glow curves of the SPP 0.5% Pr^{3+} sample after preheating to various T_{stop} values between 30 and 300 °C in 10 °C steps; (**b**) IRA plots derived from the glow curves in the T_{max}-T_{stop} experiment; (**c**) corresponding T_{max}-T_{stop}/E_a–T_{stop} plot. The sample was irradiated with X-rays for 10 s before each preheating.

CPP:0.5% Pr^{3+}		SPP:0.5% Pr^{3+}		BPP:0.5% Pr^{3+}	
T_{max}, °C	E_a, eV	T_{max}, °C	E_a, eV	T_{max}, °C	E_a, eV
60	0.85 ± 0.07	65	1.01 ± 0.06	55	0.73 ± 0.16
110	1.03 ± 0.09	105	1.08 ± 0.04	110	0.94 ± 0.13
195	1.17 ± 0.10	150	1.14 ± 0.10	185	1.18 ± 0.05
240	1.30 ± 0.13	205	1.31 ± 0.06	290	1.34 ± 0.07
300	1.52 ± 0.15	285	1.69 ± 0.05		

Table 2. Glow peak temperatures and activation energies for 0.5% Pr^{3+}-doped CPP, SPP, and BPP.

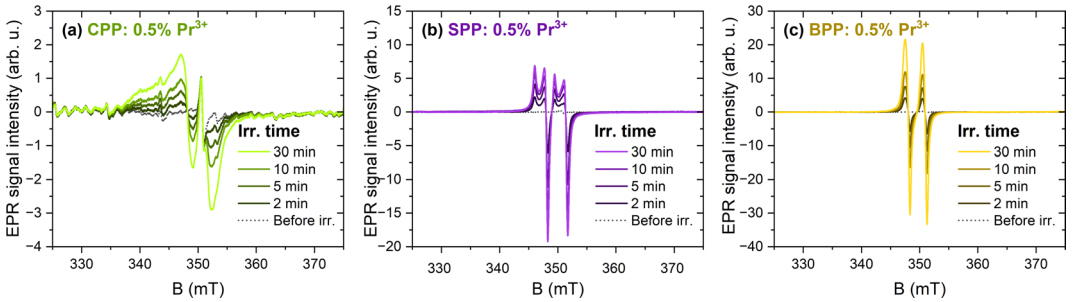

Fig. 9. EPR spectra (RT, 10 mW) of 0.5% Pr^{3+}-doped (**a**) CPP, (**b**) SPP, and (**c**) BPP samples before and after irradiation with X-rays.

To estimate the trap depths, IRA was applied to the low-temperature side of the glow peaks observed in the T_{max}–T_{stop} experiment. In this region, the signal intensity follows Arrhenius-type behaviour (Eq. (1)), allowing the extraction of E_a without assuming a kinetic order.

$$I(T) = C \cdot exp\left(-\frac{E_a}{k_B T}\right) \tag{1}$$

Here, $I(T)$ is the TSL intensity as a function of temperature; C is a temperature-independent constant that includes the frequency factor; k_B is the Boltzmann constant; T is temperature. According to Eq. (1), plotting $ln(I)$ against $(k_B T)^{-1}$ yields a straight line during the early part of the glow-peak rise. The slope of this line equals $-E_a$, enabling straightforward determination of the trap depth. As summarised in Table 2, the estimated trap depths span approximately 0.7–1.7 eV, indicating a broad distribution of traps with varying thermal stabilities.

EPR

EPR spectroscopy was applied to characterise charge trapping processes in the pyrophosphate samples. Before X-ray irradiation, the Mn^{2+} signal was detected in the CPP sample, which is a common trace impurity in calcium-containing phosphates[44,45]. In contrast, SPP and BPP samples were virtually "EPR-silent", indicating a good purity with respect to paramagnetic transition metal ions. Figure 9 reveals a dose-dependent accumulation of

radiation-induced radicals in all hosts upon X-ray exposure for selected irradiation times. EPR spectra recorded at varying microwave power levels (Fig. S6) confirm the absence of power saturation for these RT measurements.

EPR spectra of samples containing varying concentrations of Pr^{3+} ions were measured after X-ray irradiation to assess the influence of the dopant on radiation-induced charge trapping in pyrophosphates. Representative results for selected Pr^{3+} concentrations are compared in Fig. 10. Only minor X-ray-induced EPR signal intensity fluctuations with Pr^{3+} concentration are observed for the CPP samples. In contrast, the SPP and BPP series exhibit a more pronounced dependence on Pr^{3+} concentration, with the highest EPR signal intensity observed for samples containing 0.5–1.0% Pr^{3+}. The nature of paramagnetic centres in BPP samples is similar regardless of doping, suggesting that Pr^{3+} primarily influences the extent of radiation-induced charge trapping rather than the types of paramagnetic centres formed. The observed EPR intensity reflects the number of paramagnetic centres present following irradiation and may therefore arise from changes in the efficiency of charge trapping in addition to changes in the concentration of trapping defects. This behaviour may reflect a more direct involvement of the Pr^{3+} electronic states in the charge trapping processes, as discussed later in "$Sr_2P_2O_7$:0.5% Pr^{3+}" section. In SPP samples, however, Pr^{3+} incorporation leads to the formation of additional paramagnetic defects, as evidenced by the absence of the dominant EPR signal in the undoped material. At higher dopant concentrations, an additional EPR signal appears in SPP, which is likely associated with impurity phases present in these samples. A decrease in the EPR signal intensity is observed at the highest Pr^{3+} concentrations in both SPP and BPP. This reduction is likely related to defect interactions and charge compensation effects introduced by the substitution of divalent host cations with trivalent rare earth ions.

Figure S7 presents a comprehensive overview of annealing experiments obtained under different EPR acquisition conditions. RT X-band EPR spectra (Fig. S7a–c) form the basis for analysing the thermal stability of dominant paramagnetic defects discussed above. Low-temperature EPR measurements (Fig. S7d–f), where longer spin–lattice relaxation times are expected, provide improved spectral resolution and enable the detection of additional signals. Q-band EPR spectra (Fig. S7g–i) facilitate more reliable separation of magnetic field-dependent (Zeeman) and field-independent (hyperfine (HF)) contributions to the spin Hamiltonian (SH). The complex evolution of X-ray-induced EPR signals with annealing temperature in the pyrophosphates is caused by the superposition of multiple overlapping components: at least four in CPP (C1-C4), five in SPP (S1-S5), and three in BPP (B1-B3). Below, these components are deconvoluted through simultaneous multifrequency simulations of the experimental spectra using the following SH:

$$\hat{H} = g\mu_B B\hat{S} + \hat{S}A\hat{I}, \tag{2}$$

where g is the g-factor; μ_B—the Bohr magneton; B—external magnetic field; $\widehat{S}$—electronic spin operator; A—hyperfine (HF) interaction tensor; $\widehat{I}$—nuclear spin operator. The radicals were modelled as electronic spin $S = 1/2$ systems, including HF interaction with ^{31}P nuclear spins ($I = 1/2$; 100% natural abundance) where necessary. Simulations of selected components (C1, S1, B1) are presented in Fig. 11, while the full analysis is provided in the supporting information file: Figure S8—CPP (C2-C4); Figure S9—SPP (S2-S5); Figure S10—BPP (B2-B3). Table 3 summarises the fitted SH parameters for all components.

The C1, S1, and B1 signals exhibit similar spectroscopic characteristics, namely g-values exceeding the free-electron value ($g > g_e = 2.0023$) and weakly anisotropic ^{31}P HF couplings of around 80–100 MHz. Such SH parameters are characteristic of hole-type centres, where the unpaired spin resides predominantly in an oxygen 2p orbital with partial spin density transferred to a neighbouring phosphorus nucleus. These features are consistent with oxygen-centred hole radicals associated with PO_4 units in the pyrophosphate lattice. Comparable SH parameters have been reported for phosphate-related hole centres (often historically denoted as PO_4^{2-} radicals) in a variety of hosts, including phosphates, sulphates, and carbonates[18,46,47]. The observation of HF interaction with a single ^{31}P nucleus suggests that the hole is localised at one of the terminal oxygen ions of the pyrophosphate group rather than the bridging P-O-P unit, where two equivalent phosphorus nuclei would be expected. The annealing kinetics (Fig. 12) suggest that the phosphorus-related trapped hole centres are likely related to TSL glow peaks in the 25–125 °C range.

The C2, C3, C4, and B2 signals are characterised by nearly isotropic g values close to or slightly below the free-electron value ($g \leq g_e$) and considerably larger, axially symmetric ^{31}P HF couplings in the 1.4–2.6 GHz range. Such SH parameters are typical of phosphorus-centred electron-type centres, where the unpaired spin

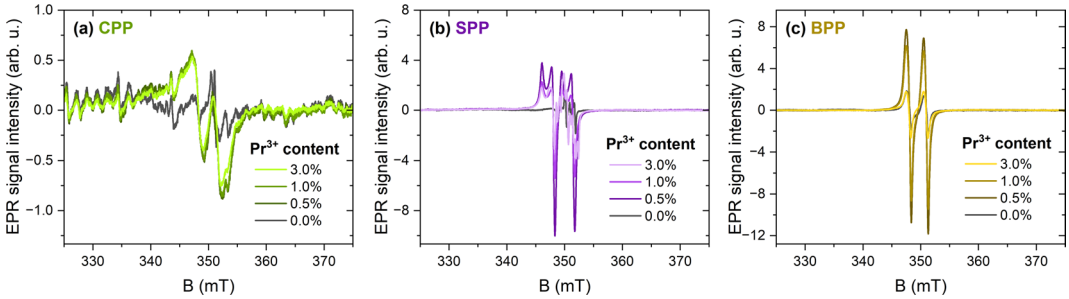

Fig. 10. EPR spectra (RT, 10 mW) of X-ray irradiated (**a**) CPP, (**b**) SPP, and (**c**) BPP samples with varying Pr^{3+} concentrations.

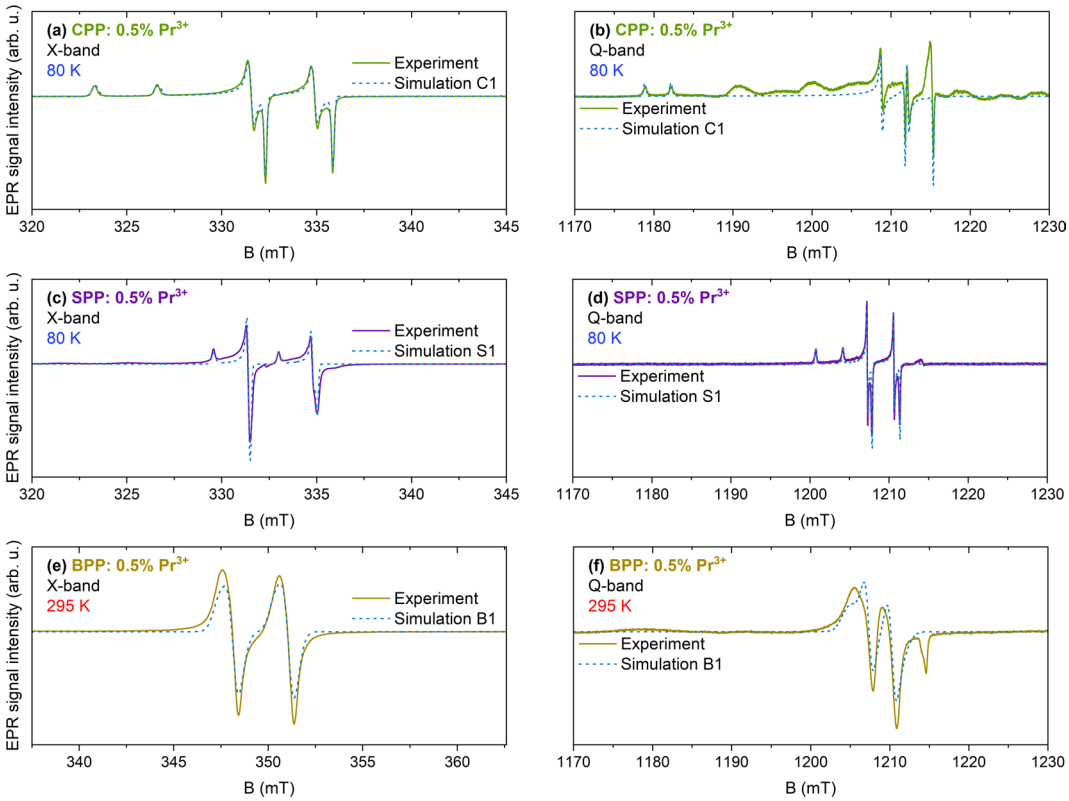

Fig. 11. Multifrequency EPR spectra simulations of 0.5% Pr^{3+}-doped (**a**, **b**; 80 K, 1 mW) CPP, (**c**, **d**; 80 K, 1 mW) SPP, and (**e**, **f**; RT, 10 mW) BPP samples after irradiation with X-rays.

Host	Radical	*g* factor			HF coupling with ^{31}P		
		g_1	g_2	g_3	A_1, MHz	A_2, MHz	A_3, MHz
CPP	C1	2.0586	2.0077	2.0025	95	94	99
	C2	2.0020	2.0009	2.0010	1518	1513	1965
	C3	2.0010	2.0010	2.0010	1648 28	1648 28	2126 25
	C4	1.9970	1.9970	1.9955	2129	2129	2637
SPP	S1	2.0195	2.0086	2.0075	97	95	99
	S2	2.0037	2.0016	1.9998	37	40	39
	S3	1.9929	1.9929	1.9929			
	S4	2.0597	2.0121	1.9971			
	S5	2.0195	2.0132	2.0132			
BPP	B1	2.0140	2.0095	2.0081	84	83	81
	B2	1.9997	1.9997	1.9993	1415	1415	1931
	B3	2.0105	2.0105	2.0105			

Table 3. SH parameters of X-ray-induced radicals in pyrophosphate samples.

is localised in an orbital with significant s-character, resulting in strong Fermi contact interaction with the ^{31}P nucleus. PO_3^{2-}-type species could be a likely candidate, forming due to the unpaired electron being trapped by an oxygen vacancy of a locally distorted phosphate tetrahedron[18]. The progressive increase of ^{31}P HF couplings from C2 to C3 and further to C4, together with their partially overlapping annealing kinetics (Fig. 12), suggests thermally stimulated electron transfer processes between similar charge traps in CPP. C3 is differentiated from the others by the detection of secondary EPR ^{31}P HF structure, which may indicate electron localisation near a bridging P–O–P bond. In contrast, the substantially larger HF coupling and broader linewidths of C4 and B2 suggest a highly distorted phosphate-related electron centre.

The additional EPR signals without discernible ^{31}P HF structure present in SPP (S3-S5) are less readily assigned to intrinsic phosphate-related defects. The positive g-factor shifts of S4 from the g_e value and pronounced anisotropy indicate a hole-type character. Such g-factor values are consistent with oxygen-centred radicals[18],

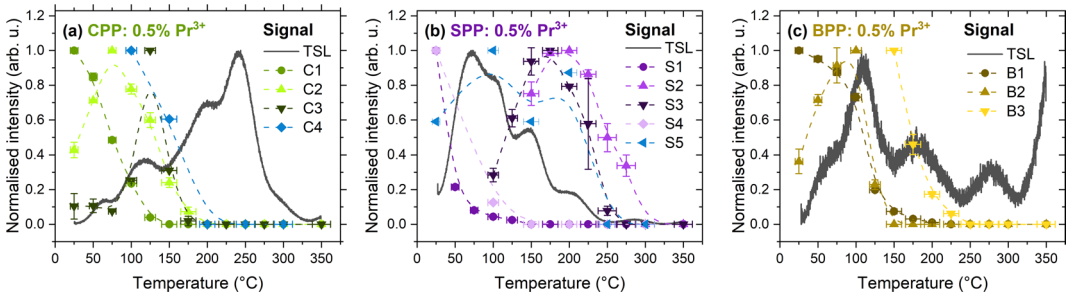

Fig. 12. Annealing kinetics of individual EPR signal components overlaid with TSL glow curves of 0.5% Pr^{3+}-doped (**a**) CPP, (**b**) SPP, and (**c**) BPP samples.

tentatively attributed to O^- species in the pyrophosphate lattice. The S3 and S5 signals exhibit more isotropic g-values and may originate from impurity-related centres or defect complexes.

TSL glow curves and paramagnetic centre thermal stabilities are comparatively presented in Fig. 12. In the investigated alkaline earth metal pyrophosphates, X-ray-induced radicals can be broadly categorised into PO_4^{2-}-type hole and PO_3^{2-}-type electron centres. The formation of these radicals suggests that the spin is predominantly delocalised within individual $[PO_4]^{3-}$ units instead of the whole $[P_2O_7]^{4-}$ pyrophosphate group. The annealing kinetics of X-ray induced radicals and TSL glow curves of CPP and BPP partially overlap in the 25–200 °C range, whereas recombination processes at higher temperatures likely involve non-paramagnetic defects. SPP exhibits a wider variety of paramagnetic defects and annealing ranges together with the highest integrated TSL intensity (Fig. 7b); therefore, the following section explores its potential as a persistent luminescence material.

$Sr_2P_2O_7$:0.5% Pr^{3+}

Charge trapping and recombination processes following 230 nm excitation were investigated in the 0.5% Pr^{3+}-doped pyrophosphate samples. UV irradiation produces qualitatively similar TSL glow curves (Fig. S11) and EPR spectra (Fig. S12) compared to X-ray irradiation, indicating that analogous trapping centres are populated under both excitation conditions. This suggests that photoexcitation of Pr^{3+} $4f^2 \rightarrow 4f^15d^1$ transitions (Fig. 3) leads to the generation of charge carriers that are subsequently captured at trapping sites, forming paramagnetic centres. In this context, Pr^{3+} ions may act both as luminescence centres and as charge trapping centres[28].

Among the investigated compositions, $Sr_2P_2O_7$:0.5% Pr^{3+} was selected for further study due to its relatively high integrated TSL intensity and favourable glow peak positions for efficient persistent luminescence. The upper panels of Fig. 13 present UV-excited persistent luminescence behaviour correlated with EPR spectroscopy, while the lower panels illustrate the effect of subsequent 420 nm optical stimulation on paramagnetic centres and charge traps.

$Sr_2P_2O_7$:0.5% Pr^{3+} exhibits long-lasting persistent luminescence in the UV–VIS spectral range, with high emission intensity (Fig. 13b). The persistent luminescence spectrum (inset of Fig. 13b) closely resembles the photoluminescence spectrum (Fig. 3) and consists of emission lines corresponding to the characteristic 4f-4f visible and 5d4f-4f UV-C optical transitions of Pr^{3+} ions. Persistent luminescence decay was detectable for more than 16 h using a standard PMT system in a laboratory setting. Moreover, emission power density during the first minutes following excitation is in the 2.8–0.3 mW/m^2 range, with comparable contributions from UV and VIS spectral regions (Fig. S13), placing this material among the more competitive UV persistent phosphors reported to date[32,48,49]. Persistent luminescence decay does not perfectly follow a linear trend in a double logarithmic plot, indicating that the recombination process involves multiple pathways and a distribution of trapping states, consistent with the complex trap distribution revealed by the TSL data in Fig. 8.

The decay of EPR spectra at room temperature (Fig. 13a) indicates that phosphorus-related hole traps are involved in the persistent luminescence process of SPP:Pr^{3+}. The S1 signal, attributed to PO_4^{2-}-type radicals, decreases to below 20% of its initial intensity within one day following 230 nm excitation (inset of Fig. 13a). The EPR signal decay-rate, calculated as the first derivative of integrated intensity, is overlaid on persistent luminescence kinetics in Fig. 13b. The order-of-magnitude similarities in the temporal evolution of both the EPR decay rate and persistent luminescence intensities suggest a direct correlation between the annihilation of these paramagnetic centres and recombination luminescence. Under 230 nm excitation, Pr^{3+} ions are excited via $4f^2 \rightarrow 4f^15d^1$ transitions and, if the excited 5d state lies close to the conduction band, electron delocalisation may occur, leading to charge carrier trapping. In this scenario, Pr^{3+} may transiently participate in the charge separation process, acting as a hole trap. A plausible mechanism involves initial hole localisation at Pr^{3+} ($Pr^{3+} \rightarrow Pr^{4+}$), followed by hole transfer to a nearby phosphate group resulting in the formation of the PO_4^{2-}-type centres detected by EPR.

UV-induced paramagnetic centres in SPP:Pr^{3+} can be stimulated both thermally and optically. Figure 13c shows that within 20 min of UV excitation, the double-integrated EPR signal intensity decreases to 81% of its initial value if the sample is kept in the dark (upper traces) and to 36% when additional blue-light stimulation is applied. In contrast, TSL glow curves (Fig. 13d) exhibit a stronger response to optical stimulation, with the signal intensity reduced to approximately 10% of its initial value. The shallow traps are preferentially depleted under optical stimulation, resulting in a redistribution of the relative glow peak intensities. The discrepancy between the stimulation efficiency of the relatively unstable S1 EPR signal and shallow traps observed in the

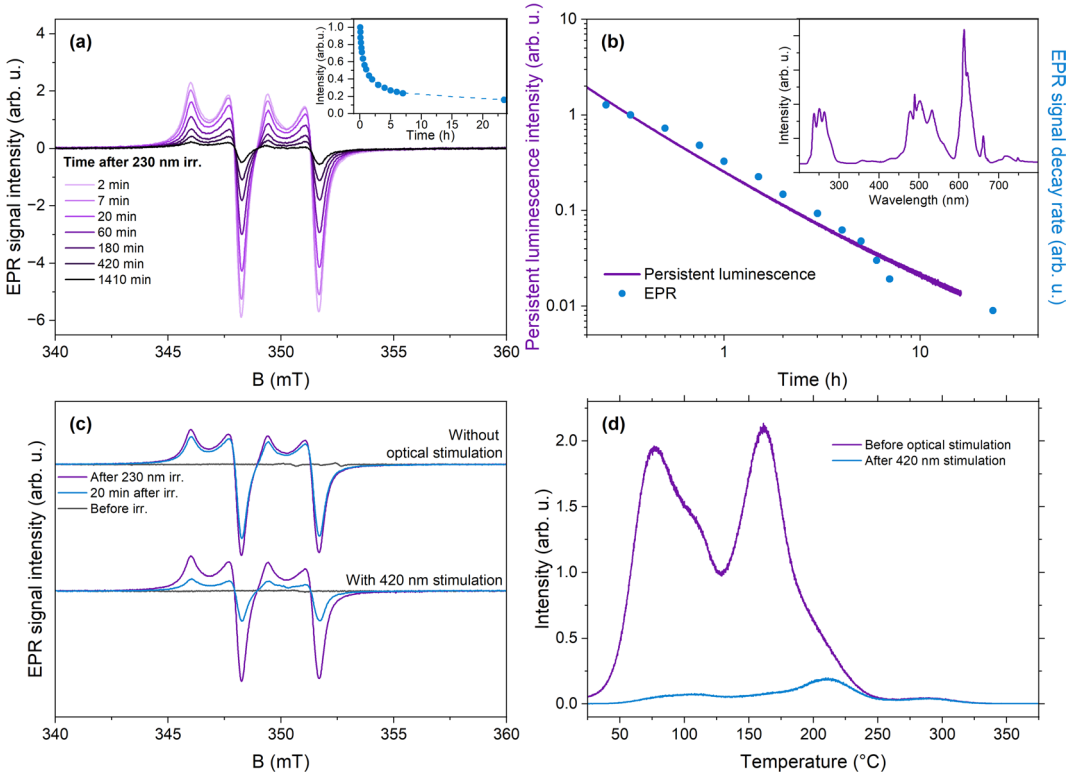

Fig. 13. EPR, persistent luminescence, and optical stimulation of SPP:0.5% Pr^{3+} following 230 nm laser excitation: (**a**) temporal decay EPR spectra and double-integrated intensities; (**b**) persistent luminescence kinetics overlaid with EPR signal decay rate (both normalised at 30 min); inset: persistent luminescence spectrum; (**c**) EPR spectra and (**d**) TSL glow curves measured without and with 420 nm stimulation.

TSL data hints at the complex nature of charge trapping and recombination processes in SPP. If the EPR signal corresponds to a PO_4^{2-}-type centre, its decay implies recombination with electrons released from optically stimulated trapping states. The partial reduction of the EPR signal indicates that only a subset of electron traps can be emptied at the stimulation wavelength, while others remain inactive. Conversely, the near-complete depletion of shallow TSL peaks suggests that not all EPR-active centres act as radiative recombination partners. The ability to selectively manipulate charge trapping states via optical stimulation highlights the potential of SPP for tuneable luminescence applications.

Observation of charge trapping under 230 nm excitation (Figs. S11 and S12) together with blue-light-driven upconversion luminescence (Fig. 5) raises the intriguing possibility that trapping centres in SPP:Pr^{3+} can also be populated using blue light. Indeed, EPR and TSL measurements acquired following 444 nm irradiation (Fig. S14) confirm this hypothesis. The efficiency of generating the PO_4^{2-}-type radicals and populating shallow trapping states via the upconversion pathway is approximately 5–7% of that achieved under direct excitation of Pr^{3+} $4f^2 \rightarrow 4f^15d^1$ transitions. During blue-light irradiation, however, charge trapping and optical stimulation of previously filled traps may occur simultaneously. Consequently, the measured trap population represents the net result of these competing processes, which may contribute to the comparatively low charging efficiency observed under upconversion excitation. Although the charging efficiency is comparatively low, the ability to generate UV–VIS persistent luminescence using blue-light excitation is notable and may provide opportunities for the development of optically rechargeable persistent phosphors.

In summary, the correlated EPR and luminescence investigations reveal that charge trapping and recombination processes in alkaline earth pyrophosphates are governed by a complex interplay between intrinsic phosphorus-related electron and hole traps and the electronic structure of the dopant ion. Among the studied materials, SPP:Pr^{3+} exhibits especially promising UV–VIS persistent luminescence performance. Further improvement of its luminescence properties may be achieved via defect engineering. For example, co-doping with Li^+ has been demonstrated to improve the phase purity and photoluminescence intensity of Pr^{3+}-doped SPP at higher dopant concentrations[17]. More generally, monovalent co-dopants such as Li^+, Na^+, and K^+ can provide charge compensation for trivalent lanthanides[9] and may modify or introduce additional charge trapping pathways, thereby influencing persistent luminescence. Alternatively, synthesis in an oxygen-deficient atmosphere could facilitate the formation of oxygen vacancies and reduced phosphate units, e.g., PO_3^{2-}- or PO_2^--type centres, which may act as electron trapping sites. Our results also indicate that the presence of deep traps in pyrophosphates limits the release of stored energy at ambient temperature. Compositional or structural modifications of these materials affecting the band structure and trap activation energies may further improve persistent luminescence performance.

Conclusions

A comprehensive comparative overview of defect-mediated luminescence processes in praseodymium-activated alkaline earth pyrophosphates ($X_2P_2O_7$; X = Ca, Sr, Ba) is presented using structural and luminescence spectroscopy techniques. Single-phase materials are obtained up to 1.0% Pr^{3+}, indicating limited dopant solubility. The Pr L_3-edge XANES studies confirm that the oxidation state of praseodymium ions is predominantly 3+. Pr^{3+} acts as an efficient luminescence centre in all investigated $X_2P_2O_7$ hosts, exhibiting both UV and visible photoluminescence emission, while $Sr_2P_2O_7$ and $Ba_2P_2O_7$ additionally show two-photon upconversion under 444 nm excitation. Pr^{3+} incorporation in alkaline earth pyrophosphates involves substitution at multiple crystallographic sites, accompanied by charge-compensating defects and local structural variations.

Combined TSL and EPR analyses following either X-ray or UV-C excitation reveal composition-dependent charge trapping in the investigated pyrophosphates. Multiple semi-overlapping trapping states with activation energies in the 0.7–1.7 eV range are observed in all materials, while the relative trap populations and recombination efficiencies differ significantly between hosts. The dominant radiation-induced defects are assigned to phosphorus-related hole (PO_4^{2-}-type) and electron (PO_3^{2-}-type) centres, demonstrating that charge localisation occurs primarily within individual PO_4 units rather than the P_2O_7 group.

Among the investigated compounds, $Sr_2P_2O_7$:Pr^{3+} exhibits the most efficient filling of the shallow traps, which are relevant to persistent luminescence. The obtained results suggest that the excitation process involves the photoionisation of Pr^{3+} to Pr^{4+}, followed by hole transfer to a nearby PO_4-unit. However, discrepancies between the depletion of shallow TSL signals and EPR-active centres under optical stimulation indicate that additional, possibly EPR-silent, species contribute to charge trapping and recombination. Overall, $Sr_2P_2O_7$:Pr^{3+} demonstrates competitive UV–VIS persistent luminescence radiance intensity with a unique excitation pathway via 444 nm upconversion and potential for further improvement by compositional modifications of the material.

Data availability

All data generated or analysed during this study are included in this published article (and its Supplementary Information file).

Received: 10 June 2026; Accepted: 10 August 2026
Published online: 13 August 2026

References

1. Chand, S., Mehra, R. & Chopra, V. Recent advancements in calcium based phosphate materials for luminescence applications. *J. Lumin.* 252, 119383 https://doi.org/10.1016/j.jlumin.2022.119383 (2022).
2. Zhao, F., Song, Z. & Liu, Q. Color-tunable persistent luminescence of $Ca_{10}M(PO_4)_7$:Eu^{2+} (M = Li, Na, and K) with a β-$Ca_3(PO_4)_2$-type structure. *Inorg. Chem.* **60**, 3952–3960. https://doi.org/10.1021/acs.inorgchem.0c03773 (2021).
3. Shan, X. et al. A narrowband ultraviolet-B-emitting $LiCaPO_4$:Gd^{3+} phosphor with super-long persistent luminescence for over 100 h. *Inorg. Chem. Front.* **11**, 8314–8323. https://doi.org/10.1039/d4qi02407a (2024).
4. Shan, X. et al. Synergistic integration of NB-UVB persistent luminescence and concentration-dependent photochromism in a phosphate phosphor for multifunctional applications. *Adv. Opt. Mater.* 13, e01335. https://doi.org/10.1002/adom.202501335 (2025).
5. Zhang, J. et al. X-ray–induced multicolor long afterglow and photostimulated luminescence from Pr^{3+}-doped $Sr_3(PO_4)_2$. *J. Am. Ceram. Soc.* 108, e20204. https://doi.org/10.1111/jace.20204 (2025).
6. Zhao, X. et al. Sunlight stimulated solar-blind ultraviolet phosphor. *Phys. Rev. Res.* **4**, L012028. https://doi.org/10.1103/PhysRevResearch.4.L012028 (2022).
7. Doke, G. et al. Excitation-selective coexistence of upconversion and persistent luminescence in Pr^{3+}-doped eulytite-type phosphates towards advanced anti-counterfeiting. *J. Mater. Chem. C* **14**, 7868–7877. https://doi.org/10.1039/d6tc00314a (2026).
8. Patel, N. P., Degda, N., Verma, V., Murthy, K. V. R. & Srinivas, M. Thermally stable photoluminescence of Eu^{3+} doped strontium pyrophosphate: red emitting phosphor with high color purity. *New J. Chem.* **48**, 5399–5411. https://doi.org/10.1039/d3nj03994c (2024).
9. Xiang, Y. et al. Deciphering defect-mediated anti-thermal quenching multimodal luminescence for information encryption. *Adv. Mater.* **38**, e15825. https://doi.org/10.1002/adma.202515825 (2026).
10. Lozano, I. B., Roman-Lopez, J., Sosa, R., Díaz-Góngora, J. A. I. & Azorín, J. Preparation of cerium doped calcium pyrophosphate: Study of luminescent behavior. *J. Lumin.* **173**, 5–10. https://doi.org/10.1016/j.jlumin.2015.12.032 (2016).
11. Roman-Lopez, J., Lozano, I. B., Cruz-Zaragoza, E., Castañeda, J. I. G. & Díaz-Góngora, J. A. I. Synthesis of β-$Ca_2P_2O_7$:Tb^{3+} to gamma radiation detection by thermoluminescence. *Appl. Radiat. Isot.* **124**, 44–48. https://doi.org/10.1016/j.apradiso.2017.03.004 (2017).
12. Li, H., Yang, Y., Li, P., Peng, D. & Li, L. Force-induced ultraviolet C luminescence of Pr^{3+}-doped $Sr_2P_2O_7$ for X-ray dosimetry. *Adv. Mater.* **36**, 2411804. https://doi.org/10.1002/adma.202411804 (2024).
13. Antuzevics, A. et al. Paramagnetic radiation-induced radicals in calcium pyrophosphate polymorphs. *Mater. Chem. Phys.* **310**, 128479. https://doi.org/10.1016/j.matchemphys.2023.128479 (2023).
14. Griesiute, D. et al. Synthesis, structural and luminescent properties of Mn-doped calcium pyrophosphate ($Ca_2P_2O_7$) polymorphs. *Sci. Rep.* **12**, 7116. https://doi.org/10.1038/s41598-022-11337-y (2022).
15. Pier, T., Schröder, F., Kappelhoff, J., Hopster, J. & Jüstel, T. On the photoluminescence of Pr(III) activated $Ca_2P_2O_7$ polymorphs. *J. Lumin.* **277**, 120934. https://doi.org/10.1016/j.jlumin.2024.120934 (2025).
16. Lin, T. et al. X-ray induced long afterglow luminescence from UVC to red region in $Ca_2P_2O_7$:Pr^{3+}. *J. Rare Earths* **43**, 1601–1606. https://doi.org/10.1016/j.jre.2024.08.012 (2025).
17. Steinbach, R., Ohlsen, A., Pier, T. & Jüstel, T. On the Pr^{3+} activated and Li^+ co-doped α-$Sr_2P_2O_7$ for high-energy excitation. *J. Lumin.* **293**, 121840. https://doi.org/10.1016/j.jlumin.2026.121840 (2026).
18. Marfunin, A. S. *Spectroscopy, Luminescence and Radiation Centers in Minerals* (Springer Science & Business Media, 2012).
19. Caliebe, W. A., Murzin, V., Kalinko, A. & Görlitz, M. High-flux XAFS-beamline P64 at PETRA III. *AIP Conf. Proc.* **2054**, 060031. https://doi.org/10.1063/1.5084662 (2019).
20. Kalinko, A. XAESA. https://gitlab.desy.de/aleksandr.kalinko/xaesa (2026).
21. Wang, X., Chen, Y., Liu, F. & Pan, Z. Solar-blind ultraviolet-C persistent luminescence phosphors. *Nat. Commun.* **11**, 2040, https://doi.org/10.1038/s41467-020-16015-z (2020).

22. Stoll, S. & Schweiger, A. EasySpin, a comprehensive software package for spectral simulation and analysis in EPR. *J. Magn. Reson.* **178**, 42–55. https://doi.org/10.1016/j.jmr.2005.08.013 (2006).
23. Shannon, R. D. Revised effective ionic radii and systematic studies of interatomic distances in halides and chalcogenides. *Acta Crystallogr. A* **32**, 751–767. https://doi.org/10.1107/S0567739476001551 (1976).
24. Boudin, S., Grandin, A., Borel, M. M., Leclaire, A. & Raveau, B. Redetermination of the β-$Ca_2P_2O_7$ structure. *Acta Crystallogr. C.* **49**, 2062–2064. https://doi.org/10.1107/S0108270193005608 (1993).
25. Hagman, L.-O., Jansson, I., Magnéli, C., Tolboe, O. & Paasivirta, J. The crystal structure of alpha-$Sr_2P_2O_7$. *Acta Chem. Scand.* **22**, 1419–1429. https://doi.org/10.3891/acta.chem.scand.22-1419 (1968).
26. ElBelghitti, A. A., Elmarzouki, A., Boukhari, A. & Holt, E. M. σ-dibarium pyrophosphate. *Acta Crystallogr. C* **51**, 1478–1480. https://doi.org/10.1107/S0108270195001739 (1995).
27. Krieke, G. et al. Structure and persistent luminescence of novel Pr-doped $Mg_3Lu_2Ge_3O_{12}$ garnet. *J. Alloys Compd.* **957**, 170421. https://doi.org/10.1016/j.jallcom.2023.170421 (2023).
28. Nilova, D. et al. Ultraviolet-C persistent luminescence and defect properties in $Ca_2Al_2SiO_7$:Pr^{3+}. *J. Lumin.* **263**, 120105. https://doi.org/10.1016/j.jlumin.2023.120105 (2023).
29. Bianconi, A. et al. Specific intermediate-valence state of insulating 4f compounds detected by L_3 x-ray absorption. *Phys. Rev. B* **35**, 806–812. https://doi.org/10.1103/PhysRevB.35.806 (1987).
30. Damdee, B. et al. Concentration-dependent physical, optical, and photoluminescence features of Pr^{3+}-doped borate glasses. *Rad. Phys. Chem.* **225**, 112092. https://doi.org/10.1016/j.radphyschem.2024.112092 (2024).
31. Rocca, F. et al. Extended X-ray absorption fine structure measurements of the local environment of Pr^{3+} ions in silica xerogels and zinc borate glasses. *J. Non. Cryst. Solids* **232–234**, 581–586. https://doi.org/10.1016/S0022-3093(98)00526-2 (1998).
32. Antuzevics, A. et al. Role of paramagnetic aluminum hole centers in UV–C persistent luminescence of $Ca_2Al_2SiO_7$:Pr^{3+}. *J. Phys. Chem. C* **128**, 21846–21854. https://doi.org/10.1021/acs.jpcc.4c06848 (2024).
33. Dramićanin, M. D. et al. Pr^{3+} visible to ultraviolet upconversion for antimicrobial applications. *Nanomaterials* **15**, 562. https://doi.org/10.3390/nano15070562 (2025).
34. Auzel, F. Upconversion and anti-Stokes processes with f and d ions in solids. *Chem. Rev.* **104**, 139–174. https://doi.org/10.1021/cr020357g (2004).
35. Xu, S., Liu, S., Zhao, C., Han, T. & Zhu, D. Luminescent properties of single-phase $Ba_2P_2O_7$:Tb^{3+}, R (R = Eu^{2+}, Ce^{3+}) phosphors for white LED. *J. Mater. Sci.: Mater Electron.* **28**, 10061–10066. https://doi.org/10.1007/s10854-017-6766-0 (2017).
36. Yu, J., Fan, Y., Wu, L., Sun, B. & Wu, Y. First-principles investigation of electronic structure and energy level scheme of phosphors: The lanthanide-doped $Sr_2P_2O_7$. *ECS J. Solid State Sci. Technol.* **10**, 056004. https://doi.org/10.1149/2162-8777/abfc27 (2021).
37. Srivastava, A. M., Jennings, M. & Collins, J. The interconfigurational ($4f^15d^1$→$4f^2$) luminescence of Pr^{3+} in $LuPO_4$, $K_3Lu(PO_4)_2$ and $LiLuSiO_4$. *Opt. Mater.* **34**, 1347–1352. https://doi.org/10.1016/j.optmat.2012.02.016 (2012).
38. Rebrova, N. et al. Luminescence and upconversion properties of a novel ultraviolet-C emitting phosphor: Rb_2NaYF_6:Pr^{3+}. *J. Mater. Chem. C* **13**, 23650–23658. https://doi.org/10.1039/D5TC03053F (2025).
39. Rebrova, N., Zdeb, P. & Dereń, P. J. Synthesis and upconversion luminescence of $LiY_9(SiO_4)_6O_2$ phosphor doped with Pr^{3+}. *J. Phys. Chem. C* **128**, 9090–9098. https://doi.org/10.1021/acs.jpcc.3c08163 (2024).
40. Adachi, S. Review—photoluminescence spectroscopy of Mn^{2+}-activated phosphors: Part I fundamentals. *ECS J. Solid State Sci. Technol.* **12**, 126003. https://doi.org/10.1149/2162-8777/ad145c (2023).
41. Bos, A. J. J. Theory of thermoluminescence. *Radiat. Meas.* **41**, S45–S56 https://doi.org/10.1016/j.radmeas.2007.01.003 (2006).
42. Furetta, C. & Kitis, G. Models in thermoluminescence. *J. Mater. Sci.* **39**, 2277–2294. https://doi.org/10.1023/B:JMSC.0000019989.60268.d7 (2004).
43. McKeever, S. W. S. *Thermoluminescence of Solids* (Cambridge University Press, 1985).
44. Matković, I., Maltar-Strmečki, N., Babić-Ivančić, V., Sikirić, M. D. & Noethig-Laslo, V. Characterisation of B-tricalcium phosphate-based bone substitute materials by electron paramagnetic resonance spectroscopy. *Radiat. Phys. Chem.* **81**, 1621–1628. https://doi.org/10.1016/j.radphyschem.2012.04.012 (2012).
45. Antuzevics, A. et al. Electron paramagnetic resonance and luminescence spectroscopy of transition metal ion impurities and X-ray-induced radicals in brushite. *J. Alloys Compd.* **996**, 174779. https://doi.org/10.1016/j.jallcom.2024.174779 (2024).
46. Ryabov, I. D. & Potashnyi, I. A. EPR and ENDOR of the PO_4^{2-} radical in anhydrite, celestite and barite. *Phys. Chem. Miner.* **19**, 334–337. https://doi.org/10.1007/BF00204010 (1992).
47. Völkel, G., Windsch, W. & Urbanowitschius, W. Dynamics of the irradiation defect centers in potassium dihydrogen phosphate observed by EPR. *J. Magn. Reson.* **18**, 57–63. https://doi.org/10.1016/0022-2364(75)90222-X (1975).
48. Yang, Y. M. et al. X-ray-activated long persistent phosphors featuring strong UVC afterglow emissions. *Light Sci. Appl.* **7**, 88https://doi.org/10.1038/s41377-018-0089-7 (2018).
49. Yan, S. et al. Ultraviolet-C persistent luminescence from the Lu_2SiO_5:Pr^{3+} persistent phosphor for solar-blind optical tagging. *Dalton Trans.* **50**, 8457–8466. https://doi.org/10.1039/d1dt00791b (2021).

Acknowledgements

We acknowledge DESY (Hamburg, Germany), a member of the Helmholtz Association HGF, for the provision of experimental facilities.

Author contributions

Conceptualisation, A.A.; methodology, A.A., D.S., G.D., G.K., A.K., A.K., N.R.; formal analysis, A.A., D.S., G.D., G.K., I.P., A.K., A.K., N.R., S.P.; investigation, A.A., D.S., G.D., G.K., I.P., A.K., A.K., N.R., P.D., A.Z.; resources, A.A., A.K., A.Z.; writing—original draft preparation, A.A., D.S., G.D., G.K., A.K., N.R., A.Z.; writing—review and editing, A.A., D.S., G.D., G.K., I.P., A.K., A.K., N.R., P.D., S.P., A.Z.; supervision, A.A.; funding acquisition, A.A. All authors reviewed the manuscript.

Funding

This research is funded by the Latvian Council of Science, postdoctoral research project No. 1.1.1.9/LZP/1/24/013 "Ultraviolet persistent luminescence in biocompatible phosphates: defect studies in novel materials". D. Salnajs gratefully acknowledges the financial support from the European Regional Development Fund and Latvian state budget grant in the framework for the project "Strengthening the doctoral research and development capacity of the University of Latvia in smart specialization areas" No 1.1.1.8/1/24/I/003. N. Rebrova acknowledges the financial support from the National Science Centre of Poland (NCN) under grants No. UMO-2025/57/B/ST4/00594.

Declarations

Competing interests
The author(s) declare no competing interests.

Additional information
Supplementary Information The online version contains supplementary material available at https://doi.org/10.1038/s41598-026-66772-y.

Correspondence and requests for materials should be addressed to A.A.

Reprints and permissions information is available at www.nature.com/reprints.

Publisher's note Springer Nature remains neutral with regard to jurisdictional claims in published maps and institutional affiliations.

Open Access This article is licensed under a Creative Commons Attribution-NonCommercial-NoDerivatives 4.0 International License, which permits any non-commercial use, sharing, distribution and reproduction in any medium or format, as long as you give appropriate credit to the original author(s) and the source, provide a link to the Creative Commons licence, and indicate if you modified the licensed material. You do not have permission under this licence to share adapted material derived from this article or parts of it. The images or other third party material in this article are included in the article's Creative Commons licence, unless indicated otherwise in a credit line to the material. If material is not included in the article's Creative Commons licence and your intended use is not permitted by statutory regulation or exceeds the permitted use, you will need to obtain permission directly from the copyright holder. To view a copy of this licence, visit http://creativecommons.org/licenses/by-nc-nd/4.0/.

© The Author(s) 2026